Multitemporal UAV-based photogrammetry for landslide detection and monitoring in a large area: a case study in the Heifangtai terrace in the Loess Plateau of China

XU Qiang https://orcid.org/0000-0001-5894-4694; e-mail: xq@cdut.edu.cn

LI Wei-le* https://orcid.org/0000-0002-3741-8801; ✉ e-mail: whylwl01@163.com

JU Yuan-zhen https://orcid.org/0000-0001-7691-0025; e-mail: 415384857@qq.com

DONG Xiu-jun https://orcid.org/0000-0002-6960-8810; e-mail: 16704937@qq.com

PENG Da-lei https://orcid.org/0000-0002-3529-3339; e-mail: 515778136@qq.com

*Corresponding author

State Key Laboratory of Geohazard Prevention and Geoenvironment Protection, Chengdu University of Technology, Chengdu 610059, China

Abstract: With high spatial resolution, on-demand-flying ability, and the capacity for obtaining three-dimensional measurements, unmanned aerial vehicle (UAV) photogrammetry is widely used for detailed investigations of single landslides, but its effectiveness for landslide detection and monitoring in a large area needs to be investigated. The Heifangtai terrace in the Loess Plateau of China is a loess terrace that is extremely susceptible to irrigation-induced loess landslides. This paper used UAV-based photogrammetry for a series of high-resolution images spanning over 30 months for landslide detection and monitoring of the terrace with an area of 32 km². Dense and evenly distributed ground control points were established and measured to ensure the high accuracy of the photogrammetry results. The structure-from-motion (SfM) technique was used to convert overlapping images into orthographic images, 3D point clouds, digital surface models (DSMs) and mesh models. Using multitemporal differential mesh models, landslide vertical movements and potential landslides were detected and monitored. The results indicate that a combination of UAV-based orthophotos and differential mesh models can be used for flexible and accurate detection and monitoring of potential loess landslides in a large area.

Introduction

Landslides are one of the major natural hazards that cause substantial economic and human losses around the world (Scaioni et al. 2014). A good understanding of the dynamics of slope mass movement is important for reducing landslide losses and developing appropriate

mitigation measures. The continuous measurements of the surface deformation offer an effective means to better understand and characterize slope movement (Peternel et al. 2017; Demoulin 2006), which assesses, in the context of the data, the possible locations that are prone to landslides. Some accurate geodetic techniques, such as total station theodolite (TST) and global position system (GPS) techniques, are widely used to monitor the surface deformation (Demoulin 2008; Malet et al. 2002; Squarzoni et al. 2005; Demoulin 2006; Yang et al. 2007); however, such techniques often require substantial effort for implementation and acquisition if the target information is to be spatially and/or temporally densified (Demoulin 2006). Remote sensing techniques enable rapid measurement of surface changes over a large area. Recent studies on landslide detection and monitoring have shown that remote sensing techniques, such as space-borne and ground-based synthetic aperture radar (SAR) interferometry (e.g., Cigna et al. 2013; Monserrat et al. 2013; Tofani et al. 2013; Bardi et al. 2014; Raspini et al. 2015; Mateos et al. 2016), aerial and/or terrestrial laser scanning (ALS and TLS) (Buckley et al. 2008; Prokop and Panholzer 2009; Brideau et al. 2012; Jaboyedoff et al. 2012; Kenner et al. 2014), and UAV-based photogrammetry are effective methods for monitoring surface deformation (Brideau et al. 2013; Jaboyedoff et al. 2012; Prokešová et al. 2010; D'Oleire-Oltmanns et al. 2012; Kenner et al. 2014; Peternel et al. 2017).

The application of UAVs is versatile and flexible compared to space-borne and airborne remote sensing techniques (Lucieer et al. 2014), and UAVs are gaining great popularity in landslide research. Typical applications include standalone UAV deployment (Yamagishi et al. 2004; Prokešová et al. 2010; D'Oleire-Oltmanns et al. 2012; Harwin et al. 2012; Niethammer et al. 2012; Qin 2014; Chen et al. 2014; Lucieer et al. 2014; Stöcker et al. 2015; Turner et al. 2015; Al-Rawabdeh et al. 2016; Dewitte et al. 2016; Fernández et al. 2016) and/or combinations with other techniques, such as light detection and ranging (LiDAR), GPS and persistent scatter interferometry (PS-InSAR) techniques (Brückl et al. 2006; Demoulin et al. 2008; Brideau et al. 2012; Dewitte et al. 2016; Mateos et al. 2016). Turner et

al. (2015) collected a series of high-resolution images with an UAV and applied the SfM technique to create DSMs for the dynamic assessment of landslides, with margins of error of 0.05 m and 0.04 m in the horizontal and vertical directions, respectively. Fernández et al. (2016) concluded that the combination of UAV photogrammetry and geographic information systems (GISs) can yield a measurement accuracy of 0.10-0.15 m. With its high spatial resolution, on-demand-flying ability, and capacity for obtaining three-dimensional measurements, UAV-based photogrammetry is widely used for detailed investigations of single landslides, while the effectiveness of UAV-based photogrammetry for landslide detection and monitoring in a large area needs to be investigated.

Loess covers approximately 6.6% of the total area of China (approx. 63.1×10^4 km²), which is macroporous, with well-developed vertical jointing that is high susceptibility to collapse when wet (Xu et al. 2012, 2014; Zhang and Liu 2010). Loess landslides are frequent and widely distributed in China, and the Heifangtai terrace in Gansu Province is extremely prone to loess landslides due to irrigation (Xu et al. 2014). Previous studies have mainly focused on the study of the failure mechanism of loess landslides with field investigations and laboratory tests, but using multitemporal UAV images to detect and monitor loess landslides in the whole terrace has not been reported (Xu et al. 2012, 2014; Zhang and Liu 2010; Peng et al. 2018; Qi et al. 2018). In this study, the UAV-based photogrammetry method was employed to detect and monitor the surface movement in the Heifangtai terrace with an area of 32 km². The surface movement was obtained over the span of 30 months by five UAV missions (performed in January 2015, May 2016, and January, March, and May 2017).

1   Study Area

The Heifangtai terrace is located 42 km west of Lanzhou city, on the north bank of the Yellow River in Yongjing County, Gansu Province, China (Figure 1a). In the early 1960s, Heifangtai terrace was selected as the resettlement area for residents of Liujiaxia and Yanguoxia located upstream of the Yellow River due to the construction of hydropower
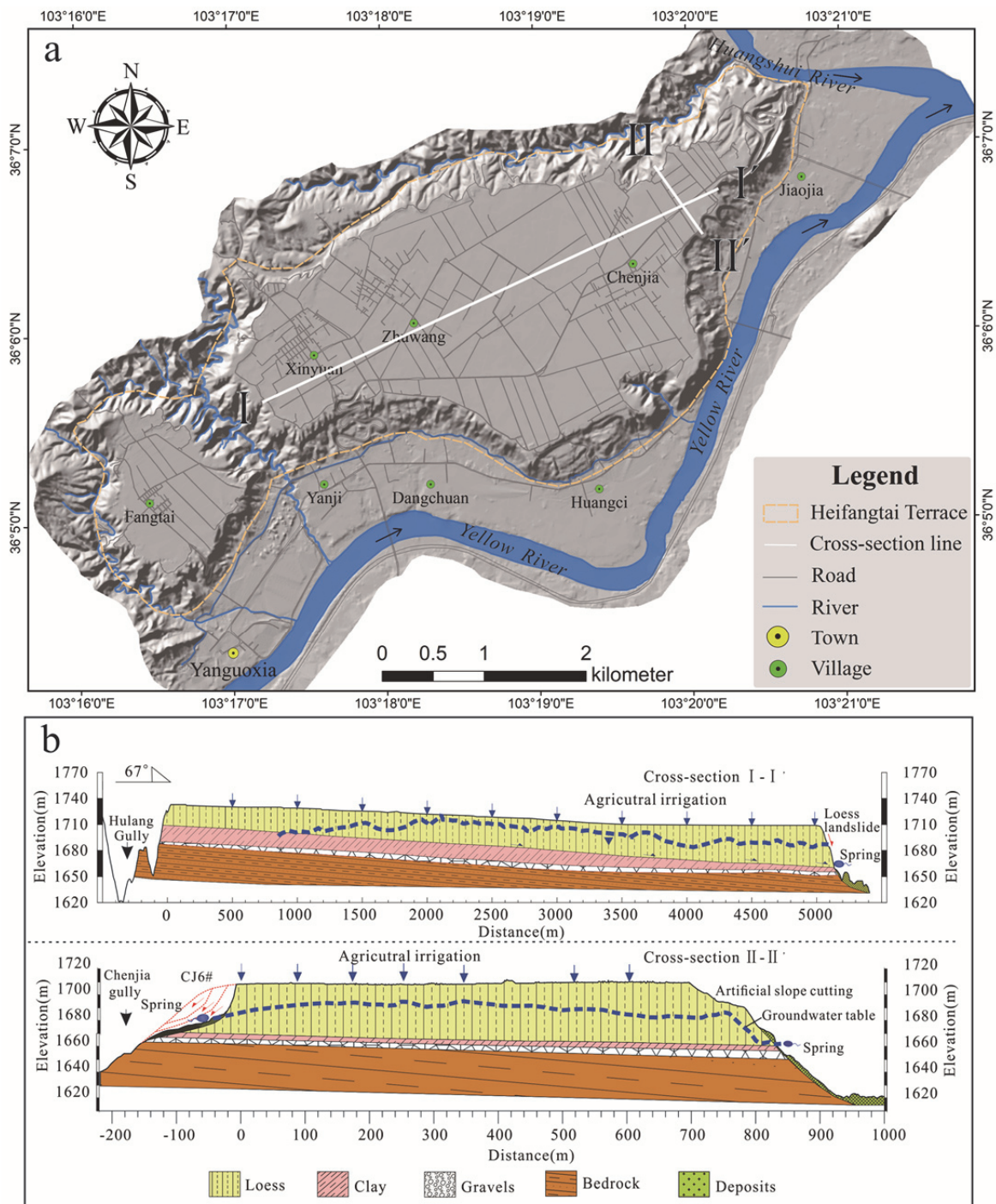
Figure 1 (a) The location of Heifangtai terrace, (b) Cross-sections of the Heifangtai terrace. I-I': the west to east section; II-II' (Peng et al. (2018)): the north to south section. The locations of the cross-sections are shown in Figure 1a.

structures. Agricultural production is a major source of income for local residents, and pumping from the Yellow River became the major source of irrigation water on the surface of Heifangtai terrace (area of irrigation: 7.6 km²).

The lithology of Heifangtai terrace comprises

the following 4 layers (Figure 1b): (1) The Holocene series landslide deposit consists of loess, gravel and sand shale, with colluvial material deposited at the toe area. (2) The Upper Pleistocene Loess (i.e., Malan loess) has a thickness of 30-50 m. The loess is largely composed of silt with cementation and a

high porosity. The open-packed fabric structure of loess makes it susceptible to collapse upon wetting. Subvertical joints are well developed in the loess layer, which provide channels for the seepage of phreatic water. (3) The Upper Pleistocene clay and gravel layer consists of overlying orange silty clay with a thickness of 3-20 m (the thickness increases from SE to NW), and the underlying gravel layer consists mainly of quartz rock and granite, which is formed by the weathering and erosion of the bedrock (with a thickness of 1-10 m). (4) The Lower Cretaceous Mudstone/Sandstone layer is the bedrock of the terrace. The thickness of the exposed rock stratum at the edge of the terrace is more than 70 m, with an average strike and dip of 135° ∠ 11°. There are on average 3-5 landslides annually at the edge of the terrace (Derbyshire et al.

1998; Derbyshire 2001; Xu et al. 2012, 2014; Zhang and Liu 2010; Peng et al. 2016). Long-term agricultural irrigation has increased the groundwater table by 20–30 m over the past five decades (Peng et al. 2019). The groundwater table increased by 20 m in the loess layer at the northern margin of the terrace, at an average rate of 0.18 m/yr (Xu et al. 2014).

2 Data and Methodology

The methodology consisted of four main steps as presented in Figure 2, which included the following steps: 1) UAV deployment for imagery acquisitions and implementations of ground control points (GCPs); 2) image processing to
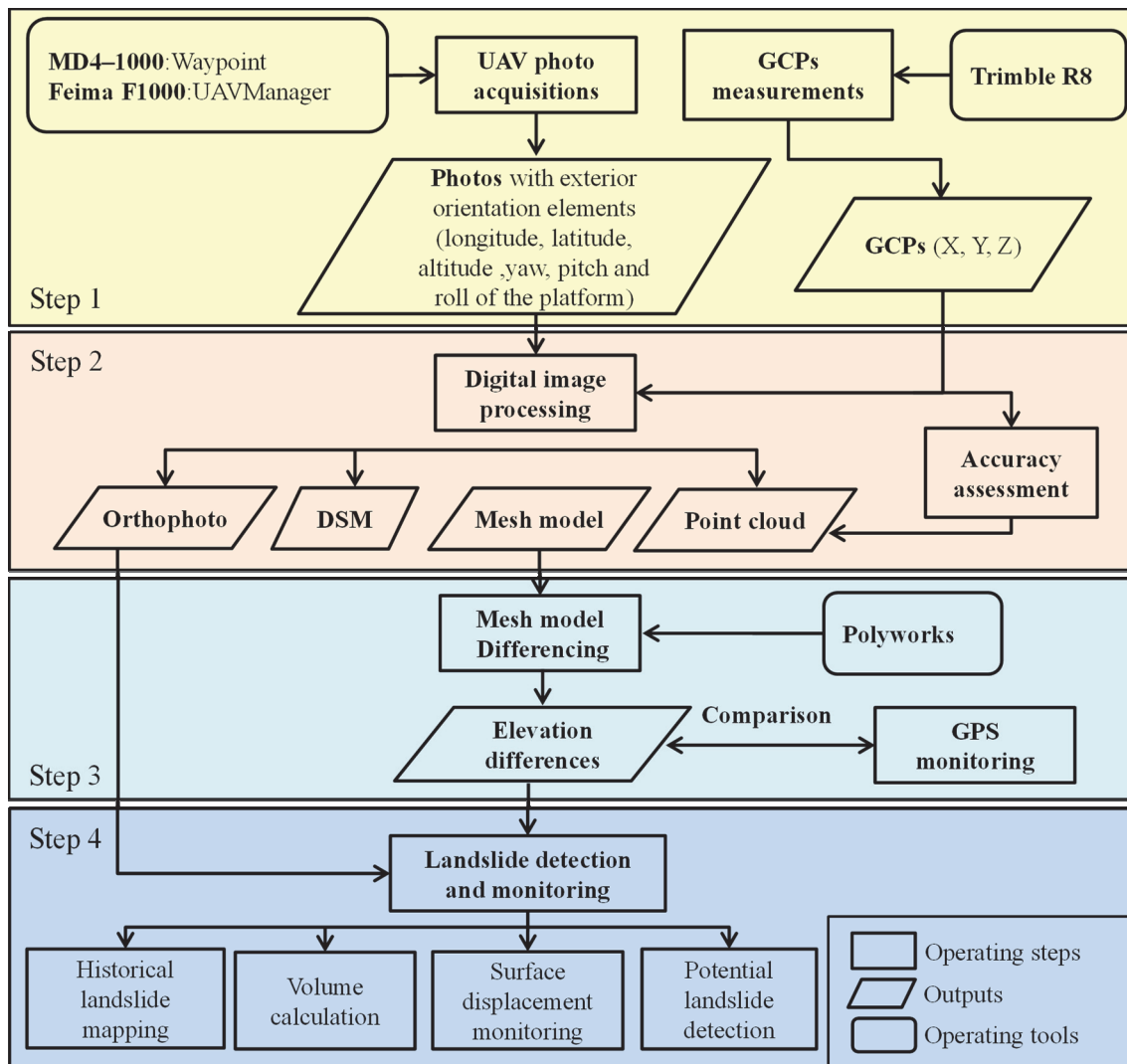

Figure 2 Flowchart of UAV data acquisition, processing, landslide identification and monitoring.

generate the orthophotos, point clouds, mesh models and DSMs of the study area; 3) calculation of the DSM offsets to obtain the spatial and temporal elevation changes; and 4) landslide detection and monitoring by the DSMs and orthophotos.

2.1 Imagery acquisitions

In this study, five UAV missions were conducted from January 2015 to May 2017. The flights were executed by using two UAV models (Table 1). The first mission covered the entire study area (32 km²), and the rest covered different sections of the terrace (Figure 1). UAV missions #1 and #2 were conducted by using a quadrocopter, MD4-1000 (Microdrones Inc., Kreuztal, Germany), which is equipped with a Sony ILCE-7R camera. MD4-1000 has a maximum takeoff weight of 6.0 kg at a cruising speed of 12 m/s, and it is guided by predefined waypoints. The average flight duration was 50 min at an average aboveground level (AGL)

of 450 m (with a resolution of 6 cm). Subsequent missions #3, #4, and #5 were performed by operating a fixed-wing UAV, Feima F1000 (Feima Robotics Ltd., Shenzhen), which was controlled manually at an average AGL of 270 m (with a resolution of 4 cm).

2.2 GCP measurements

The exterior orientation elements (X, Y, Z, yaw, pitch, and roll of the platform) were measured by the on-board GPS. Images were geo-tagged with a typical geometric accuracy of 5-10 m (D'Oleire-Oltmanns et al. 2012). As georeferencing substantially improves the accuracy, GCPs were placed prior to the flight missions, with coordinates determined by using total stations and differential global positioning systems (DGPS) (Yamagishi et al. 2004). GCPs are commonly made of artificial features located on/near more permanent structures with clear visibility from the operating UAV (Figure 3). There were 14 permanent GCPs in

Figure 3 Ground control points (GCPs) targets and their measurement by the differential global positioning systems (DGPS). (a) permanent GCP; (b) static GPS measurement; (c) natural GCP; (d) artificial GCP; (e) GCP on the road.

Table 1 An overview of the UAV imagery acquisitions

UAV missions	1st time	2nd time	3rd time	4th time	5th time
Date	January 2015	May 2016	January 2017	March 2017	May 2017
UAV drone	MD4–1000	MD4–1000	Feima F1000	Feima F1000	Feima F1000
Camera	Sony ILCE-7R	Sony ILCE-7R	Sony ILCE-5100	Sony ILCE-5100	Sony ILCE-5100
Region	Entire study area	Dangchuan and Jiaojia and Moshigou	Dangchuan and Jiaojia and Moshigou	Moshigou	Moshigou
Area	32 km²	14 km²	19 km²	4 km²	4 km²
Flight Height	450 m	450 m	270 m	270 m	270 m
Average GSD	0.06 m	0.06 m	0.04 m	0.04 m	0.04 m
Images	1600	1111	5736	750	750
Overlap	>60%	>60%	>65%	>65%	>65%
Sidelap	>80%	>80%	>80%	>80%	>80%
GCPs	39	30	103	29	30

Note: UAV=unmanned aerial vehicle; GSD= ground sampling distance; GCP=ground control point.
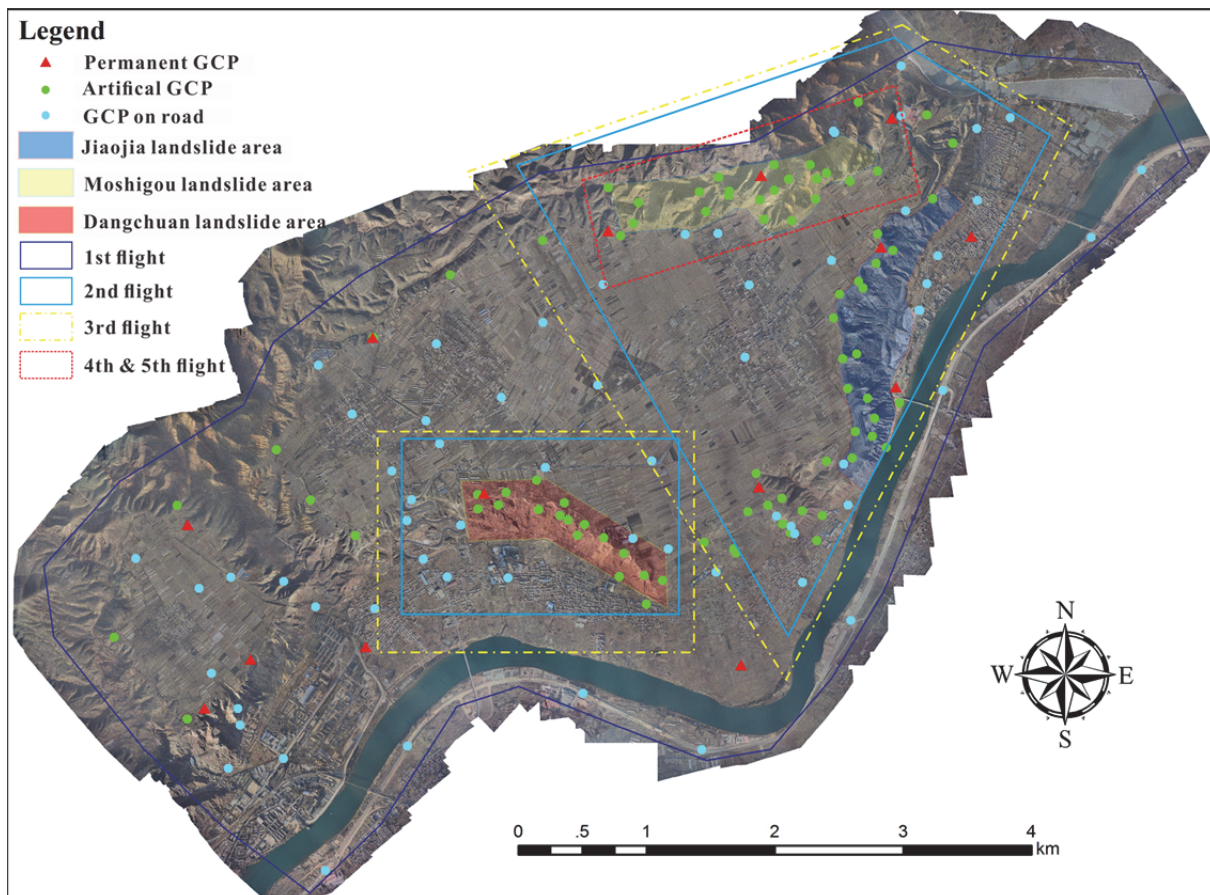

Figure 4 Distribution of the ground control points (GCPs) and the key subregions.

the study area, with an additional 82 GCPs made of artificial features and 64 GCPs on natural points on the terrace (Figure 4). The coordinates of the permanent GCPs were measured by a static GPS (Trimble R8: precision of ±10 mm), whereas the additional GCPs were measured by an RTK DGPS (precision of ±30 mm).

2.3 Image processing

The image process comprises three main steps: 1) optimizing the camera positions, analyzing the image information and extracting and matching the key points among the images; 2) constructing a 3-D point cloud and mesh model; and 3)

generating DSMs and orthomosaics. The images are processed in Pix4Dmapper (Pix4D SA, Lausanne, Switzerland) (https://pix4d.com), which utilizes the structure-from-motion (SfM) technique to construct the scene from the overlapping photos (Turner et al. 2015). The SfM process starts by acquiring images with sufficient overlap (> 60%). Based on pattern recognition algorithms, characteristic image objects can be detected and matched in the dataset (Lucieer et al. 2014). Subsequently, a bundle block adjustment is performed on the matched features to identify the position and orientation of the camera. A densification technique, i.e., multiview stereopsis (MVS) is applied to derive the dense 3-D models. The GCPs are used to georeference the 3-D model in a real-world coordinate system. Finally, the model is exported into a grid-based and/or mesh-based DSM, which derives the orthomosaics from the projected images (Lucieer et al. 2014).

2.4 Mesh model differencing

To prepare the mesh models for differencing and change detection, it is necessary to check the coregistration of each mesh model pair. As each mesh model was georeferenced during an individual workflow, it is possible that there were some minor rotational or scale differences. The mesh models were imported into Polyworks (InnovMetric Software Inc. 2010), in which an iterative closest point (ICP) algorithm was run on each pair of mesh models, and the transformation matrices that contain the rotational parameters,

translation parameters, and a scale parameter were estimated (Turner et al. 2015). For all the mesh model pairs, no rotational correction was required, and the scale factor was 1.0, implying that there were no rotational or scale differences between the mesh model pairs. The differential models of the Dangchuang area calculated by using mesh models between January 2015 and May 2016, as well as May 2016 and January 2017, are shown in Figure 5.

2.5 Accuracy assessment

The overall accuracy of the resultant dataset was assessed by GCP errors, which were obtained by comparing the GCP position from the photogrammetry to that measured by the GPS. The GCPs that were identified in the orthomosaic with errors in the x and y coordinates and the difference in their height were measured by the DSMs. A summary of the statistics, such as the minimum, maximum, mean error, and root mean squared error (RMSE), were calculated to quantify the geometric accuracies. The overall accuracy of the generated orthophoto material and DSMs for each UAV acquisition is presented in Table 2. The maximum horizontal and vertical RMSEs were 0.06 m and 0.11 m, respectively, which were obtained in the dataset acquired in January 2015. Owing to the increase in the number and rationalization in the spatial distribution of the GCPs after January 2017, the variations between the horizontal and vertical RMSEs decreased to 0.02-0.03 m.

Table 2 Summary of the horizontal and vertical errors of each data acquisition set

Date	Region	GCP/CHK Number	GCP/CHK Maximum Error (m)			GCP/CHK RMSE (m)		
			MaxX	MaxY	MaxZ	RMSX	RMSY	RMSZ
January 2015	Dangchuan	17/9	-0.08/-0.06	-0.07/-0.07	0.09/0.14	0.03/0.05	0.04/0.04	0.05/0.10
	Jiaojia	12/5	0.09/-0.08	0.06/0.10	0.07/-0.14	0.06/0.05	0.04/0.05	0.04/0.11
	Moshigou	10/5	-0.06/0.06	-0.13/0.06	0.16/0.10	0.04/0.02	0.05/0.03	0.10/0.06
May 2016	Dangchuan	11/8	-0.07/0.07	-0.04/-0.06	-0.12/0.11	0.03/0.05	0.04/0.03	0.05/0.05
	Jiaojia & Moshigou	19/18	0.08/0.07	-0.08/-0.13	0.09/0.12	0.04/0.04	0.03/0.04	0.06/0.06
January 2017	Dangchuan	34/13	-0.05/-0.08	0.06/0.06	0.09/-0.08	0.02/0.04	0.02/0.03	0.03/0.05
	Jiaojia & Moshigou	69/24	-0.04/-0.07	0.06/-0.07	0.07/-0.06	0.02/0.04	0.02/0.04	0.03/0.04
March 2017	Moshigou	29/13	0.03/-0.05	0.04/-0.07	-0.05/0.05	0.02/0.03	0.02/0.04	0.02/0.03
May 2017	Moshigou	30/15	0.04/-0.05	0.05/0.04	0.04/-0.07	0.02/0.04	0.02/0.02	0.02/0.06

Note: GCP=ground control point, CHK=check point, MaxX=maximum Error in the X direction, MaxY=maximum Error in the Y direction, MaxZ=maximum Error in the Z direction, RMSE= root mean square error, RMSX=root mean square error in the X direction, RMSY=root mean square error in the Y direction, RMSZ=root mean square error in the Z direction.
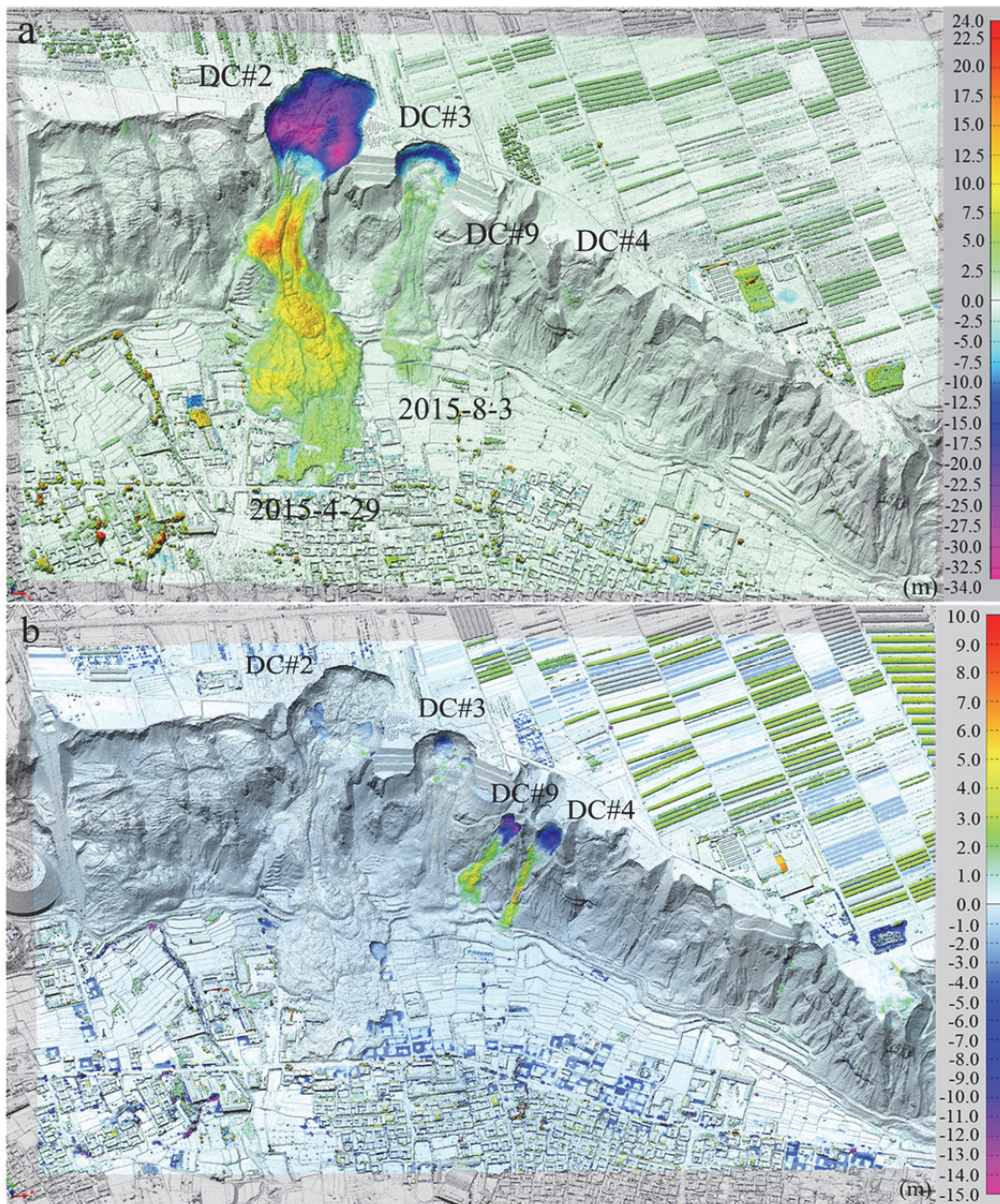
Figure 5 Differential mesh models of the Dangchuang subregion. (a) Differential model calculated using mesh models for January 2015 and the DSM for May 2016; (b) Differential model calculated using mesh models for May 2016 and the DSM for January 2017.

3   Results and Discussion

3.1 Historical landslide inventory

The historical landslides were mapped using the orthophoto generated from UAV mission #1. The scarps and deposits of historical landslides were clearly visible due to the lack of vegetation in the study area, and they could be identified by the visual interpretation of the high-resolution orthophoto (Figure 6). A total of 75 landslides were inventoried for Heifangtai terrace, of which 7 were located in the Yehu Gully, and the rest were located on the edge of the terrace. We divided the terrace into Region A (R_A) and Region B (R_B), where the landslides in R_A were mainly loess-bedrock landslides with volumes of 0.1 to 6.0 $\times 10^6$ m³, while the landslides in R_B were mainly loess landslides

with volumes of 4.9×10^3 to 2.2×10^6 m³. R_A and R_B are further divided into 6 sections, i.e., S1 (Xinyuan), S2 (Dangchuan), S3 (Huangci), S4 (Jiaojiaya), S5 (Jiaojia), and S6 (Moshigou) (Figure 7). The differences in the distribution pattern of the landslides in Heifangtai were discussed in detail by Peng et al. (2018).

3.2 Landslide volume measurement

A differential model was used to quantitatively analyze the characteristics of the landslide that occurred between two DSMs at different temporal points. Once the DSM difference was calculated, the areas of direct interest, e.g., the landslide toes and the scarps, were segmented, and the volume for each area was calculated. The height difference per pixel was multiplied by the area of a pixel and summed, thus giving a total volume in cubic meters of the landslide (Turner et al. 2015).

During our study, several loess landslides had undergone large-scale sliding, such as the DC#2 landslide (April 29, 2015), DC#3 landslide (August 3, 2015 and February 19, 2017), JJ#4 landslide (January 28, 2015), CJ#3 landslide (February 26, 2015), CJ#5 landslide (September 21, 2015), CJ#6 landslide (May 3, 2016), and CJ#8 landslide (September 20, 2015). In the case of the analysis of the DC#2 landslide that occurred on April 29, 2015 (Figure 8), the affected area of the landslide could be measured by comparing the pre- and post-failure images (Figures 9a and 9b). By analyzing the differential model (Figure 9c), the vertical displacement could be calculated for the source area as well as the accumulation area. The maximum slope surface retreat of DC#2 was estimated as 124.62 m, and the maximum width of the landslide was 164.76 m with a maximum height difference of 34.18 m. We also acquired the maximum accumulating width (187.56 m), travel distance (598.64 m), and
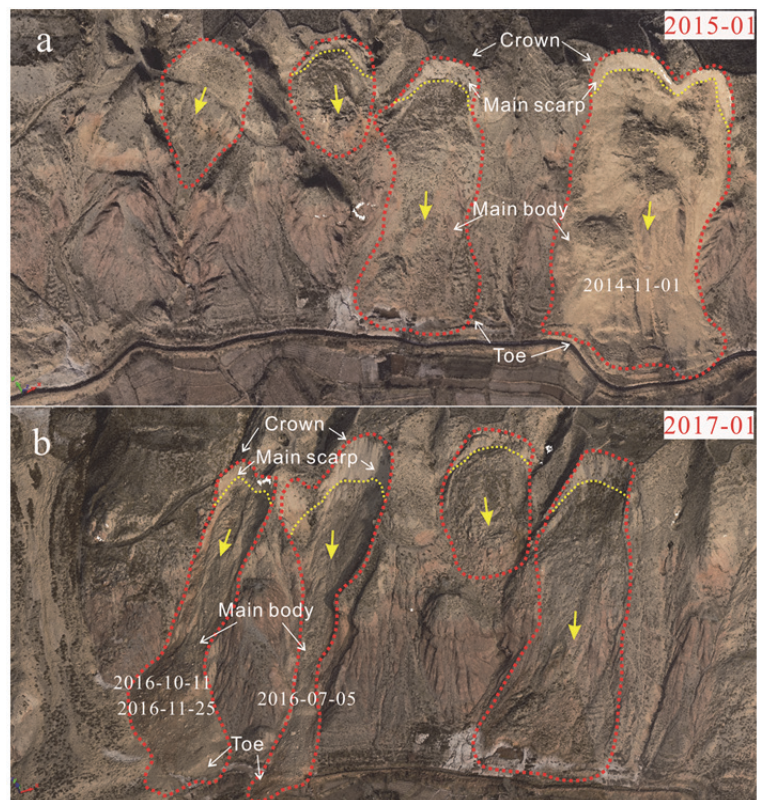

Figure 6 3D views of typical loess landslides in the study area (a) Image taken on January 2015; (b) Image taken on January 2017.
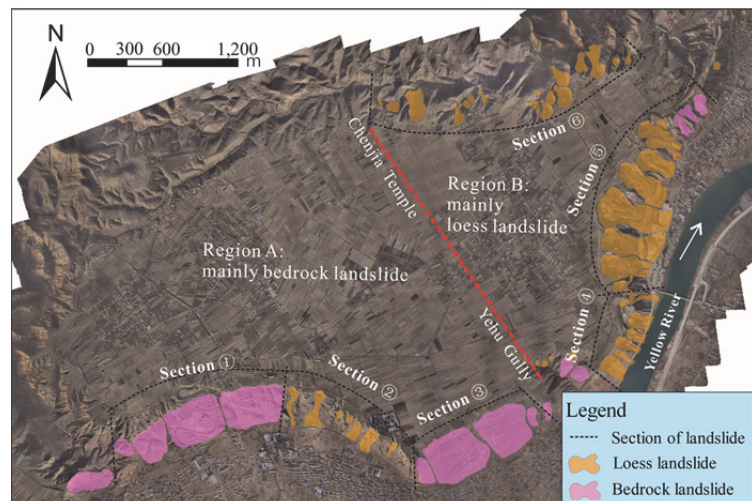

Figure 7 Historical landslides in the Heifangtai terrace.

maximum accumulation thickness (18.9 m). The sliding and accumulating volumes of the DC#2 landslide were calculated as 3.17×10^5 m³ and 4.99×10^5 m³, respectively.

3.3 Horizontal displacement monitoring
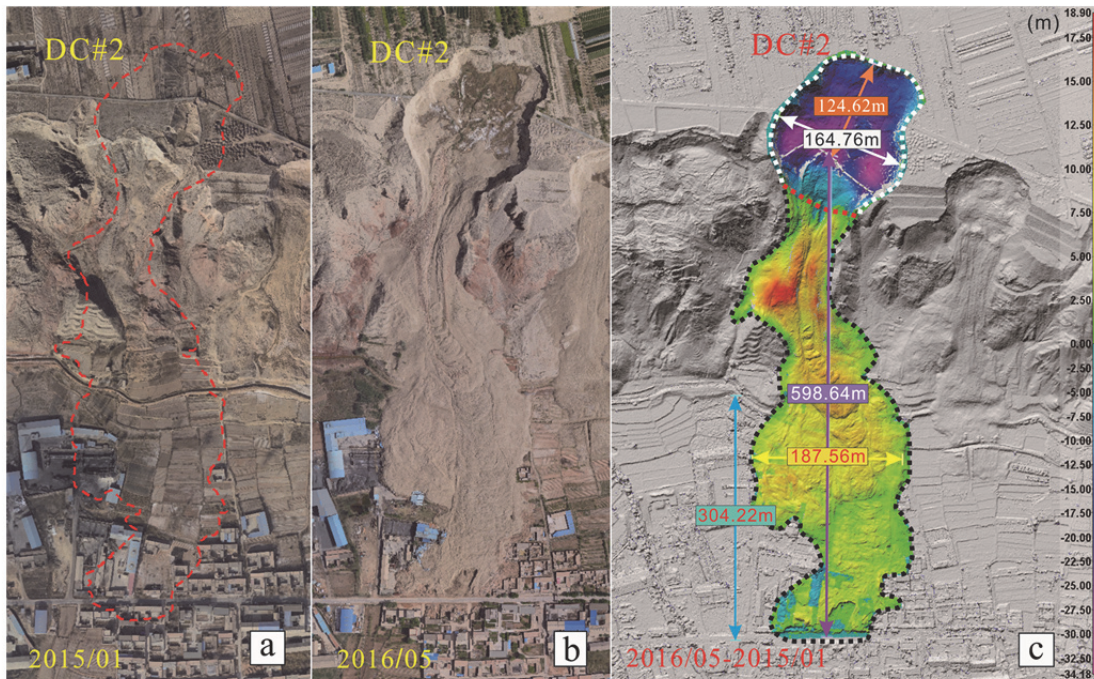
Based on the centimeter-level ground

Figure 8 Images of the DC#2 landslide. (a) unmanned aerial vehicle (UAV) image of the DC#2 landslide taken in January 2015; (b) UAV image of the DC#2 landslide taken in May 2016; (c) Differential Model of the DC#2 landslide calculated using the digital surface model (DSM) for January 2015 and DSM for May 2016.

resolution, UAV orthophotos can be used to detect and monitor the horizontal displacements of a landslide by visual interpretation. For example, two large-scale sliding events occurred during the DC#3 landslide on August 3, 2015, and February 19, 2017. The cracks and sinkholes resulting from horizontal displacement can be identified on the image (Figure 10), and the changes can be mapped using multitemporal images (Figure 10). Multistage cracks are seen in the source area, showing a tendency to develop away from the scarp. Based on the scarps of the sliding events, the locations of the tensile cracks provide some insights for estimating the potential scarp of a new landslide and, therefore, a series of estimations for the volume of the landslide.

3.4 Vertical displacement monitoring

The multitemporal differential model is used to monitor the ground deformation of landslides and is verified by ground GPS monitoring data. Figure 11a shows the differential model of the Dangchuan area between May 2016 and January 2017, in which the surface deformation at the DC#2, DC#3 and DC#4 landslides are clearly presented. A GCP point and a long-term GPS

Figure 9 The orthophoto of the DC#3 landslide taken in May 2016. The red arrow indicates the position of cracks and sinkholes around the DC#3 landslide.

monitoring station are located in this area (Figures 11b and 12d), which yields a vertical displacement of -0.7 m (Figure 11d), whereas the differential model shows a vertical displacement of -0.6 m. The overall difference between the results of the differential model and GPS is less than 0.2 m in this area.

Multitemporal models enable the dynamic monitoring of the surface deformation and provide evaluations for the early identification of landslides.
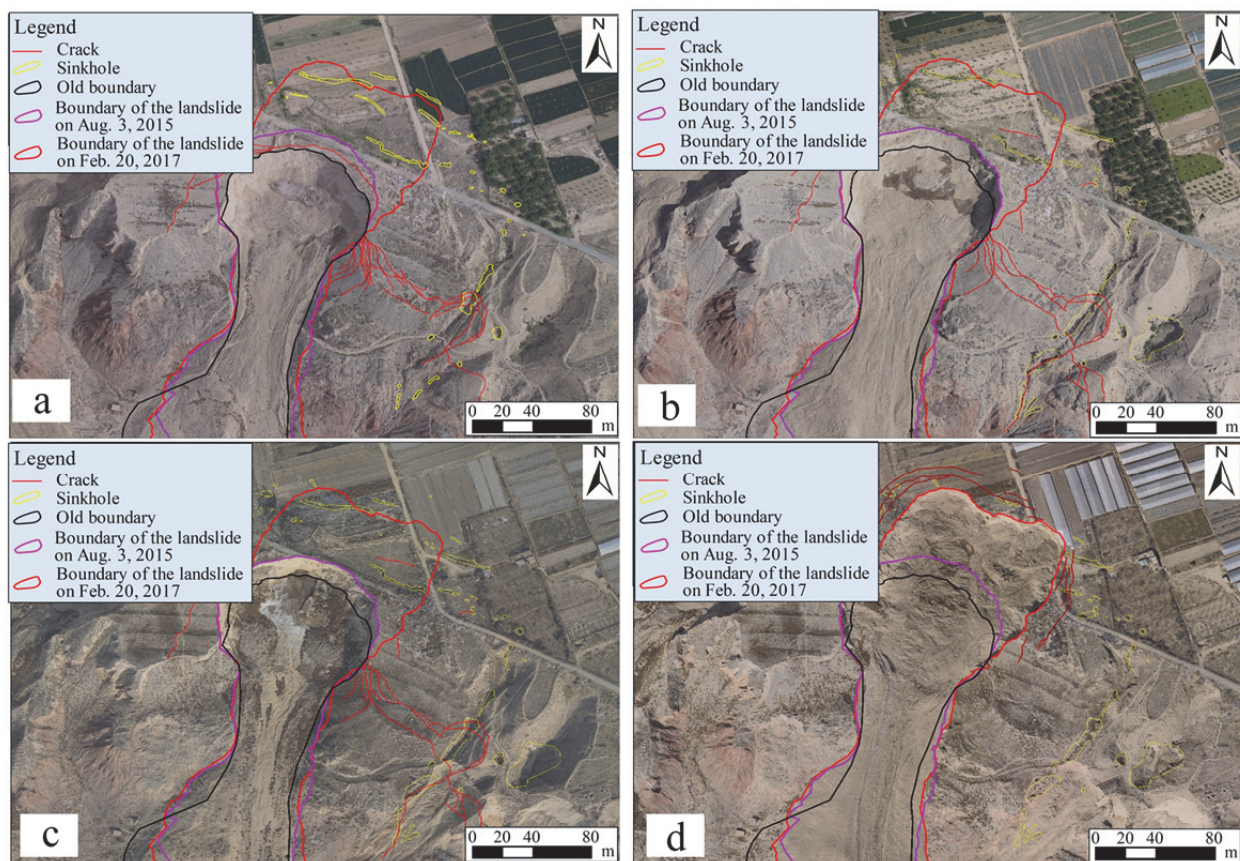
Figure 10 The horizontal monitoring results of the DC#3 landslide (a) The image taken in January 2015; (b) The image taken in May 2016; (c) The image taken in January 2017; and (d) The image taken in March 2017.

Figure 12a shows the substantial surface deformation in Dangchuan between May 2016 and January 2015, where a landslide occurred at DC#4 on July 5, 2016, and two more occurred at DC#9 on October 11 and November 11, 2016 (Figure 12). Figure 13 shows the differential mode of the CJ#6 and CJ#8 landslides; an apparent deformation occurred at CJ#6 in May 2016 and January 2017 (Figure 13a). The same phenomenon appeared for the CJ#8 landslide in March 2017 and January 2017 (Figure 13b). Figure 14c shows that small-scale landslides had occurred. This indicated that the deformation area developed into a potential landslide area before May 2017. Figure 13d shows that the deformation of the CJ#6 and CJ#8 landslides continues to develop (Figures 13e, 13f, 13g, and 13h), and these signs of deformation may indicate potential landslides at these locations.

4 Conclusions

The UAV-based photogrammetric technique

can be used for the quantitative characterization and analysis of landslides. For example, it facilitates field investigation with a more detailed understanding of the landslide, enables the integration of GIS software for hazard evaluation, and implements the geometry in the numerical simulation of the landslide compared to that of other techniques.

The key advantages of UAV-based photogrammetry for landslide detection and monitoring include a high-resolution, an on-demand deployment, and 3-D measurements; it bridges terrestrial and satellite observations. In this study, a UAV-based photogrammetry processing approach is employed to characterize the surface deformation of landslides in the Heifangtai terrace from January 2015 to May 2017. The acquired images were processed in Pix4Dmapper, and the SfM technique was used to convert overlapping images into orthophotos, 3-D point clouds, DSMs and mesh models. The accuracy was validated by using GCPs, which resulted in horizontal and vertical RMSEs of 0.06
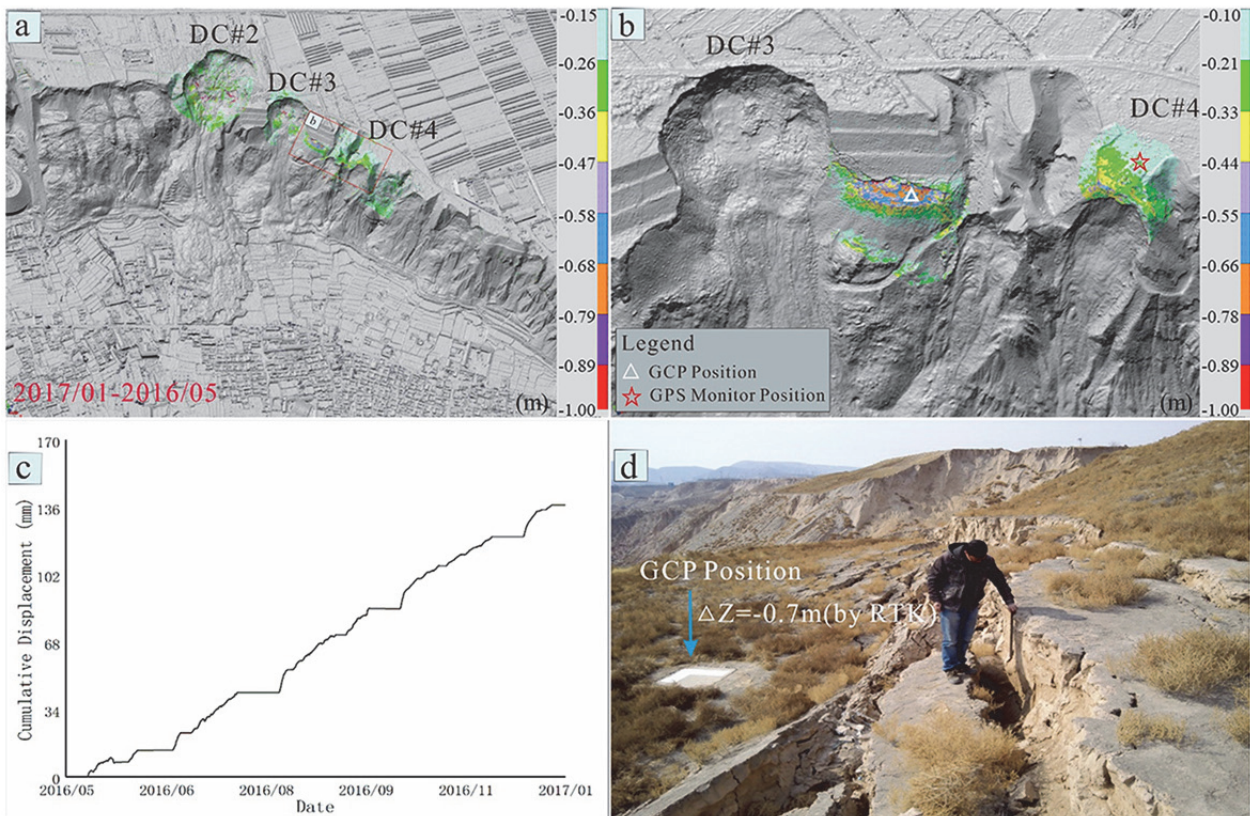
Figure 11 The vertical displacement monitoring results of the Dangchuan section. (a) Differential model of the Dangchuan section; (b) Differential model of the DC#3 and DC#4 landslides; (c) the vertical displacement obtained from GPS monitoring; (d) Photo showing the vertical displacement of the ground control points (GCPs).
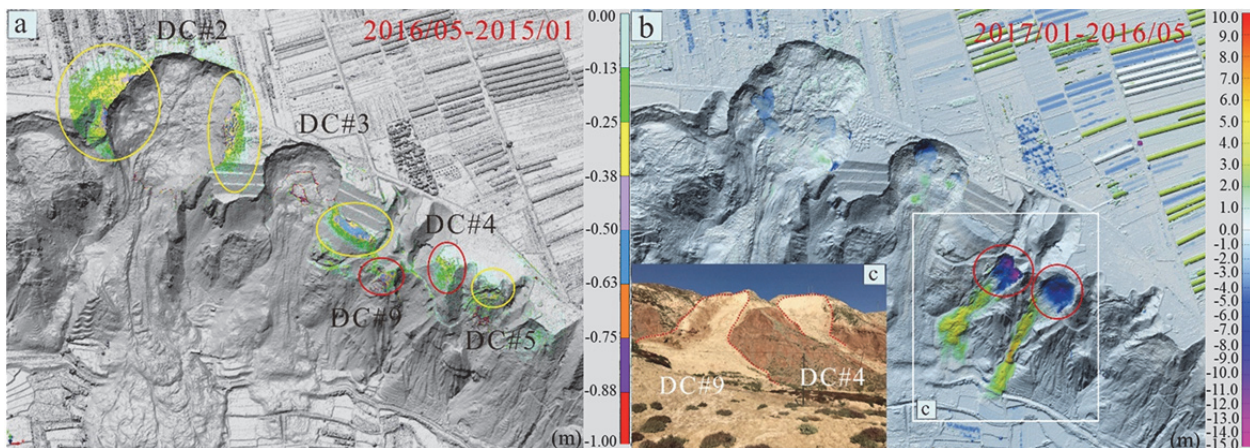

Figure 12 Differential models of the Dangchuan section. (a) Differential model of 2016/05-2015/01; (b) Differential model of 2017/01-2016/05; (c) Photo of the DC#4 and DC#9 landslides postsliding.

m and 0.11 m, respectively; however, the amount and location of the GCPs affected the accuracy. The software Polyworks was used for differencing the multidate mesh models.

There were 75 mapped landslides and horizontal displacements detected and monitored from the orthophotos. The vertical movements were monitored using differential mesh models, and some potential landslides were detected. Our results indicate that a combination of UAV-based orthophotos and differential mesh models can be used for flexible and accurate detection and monitoring of loess landslides over a large area.
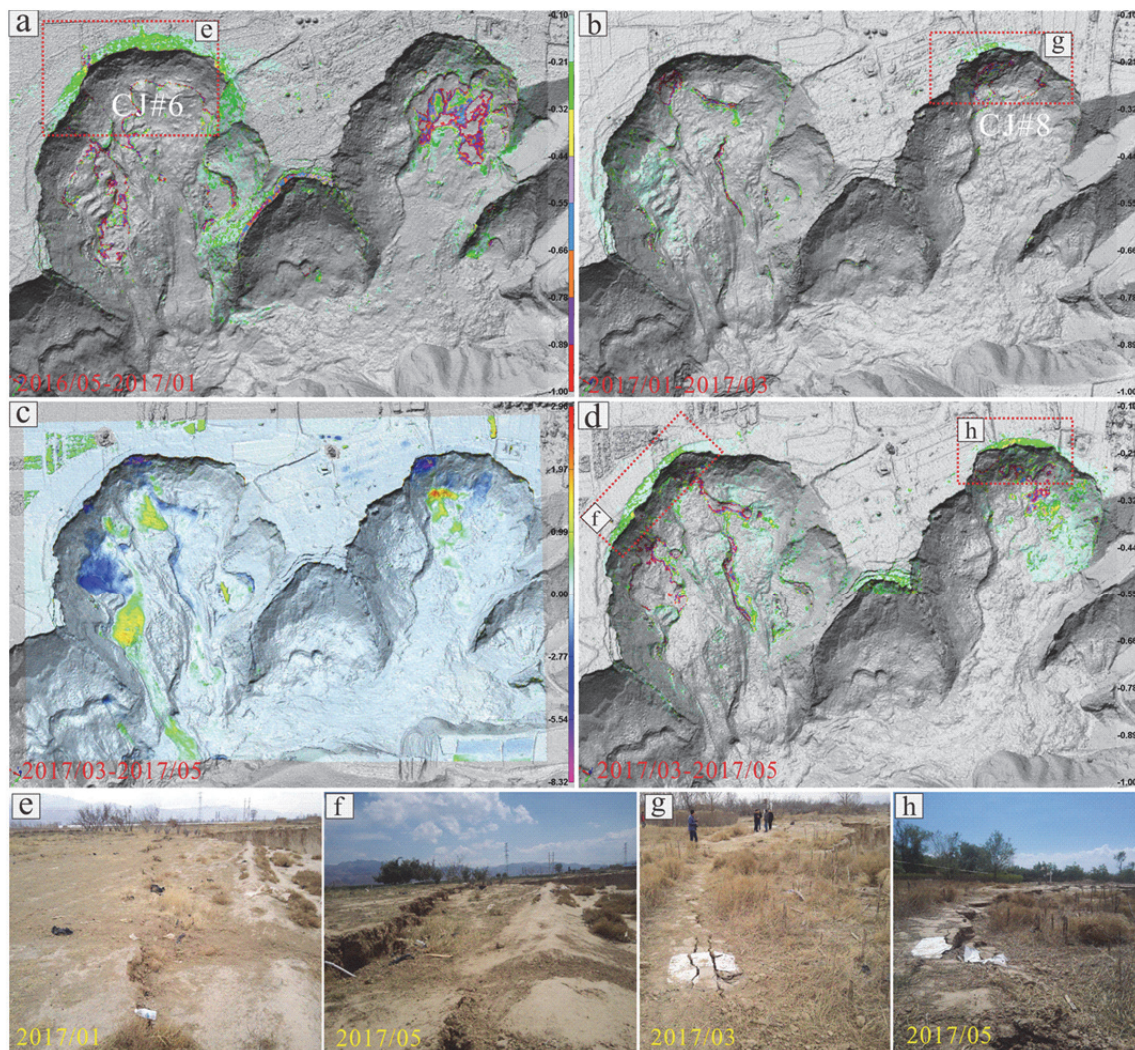
Figure 13 Differential models and photos of the CJ#6 and CJ#8 landslides. (a) Differential model of 2016/05-2017/01; (b) Differential model of 2017/01-2017/03; (c) Differential model of 2017/03-2017/05; (d) Differential model of 2017/03-2017/05; (e) and (f) Photos showing the surface deformation of the CJ#6 landslide; (g) and (h) Photos showing the surface deformation of the CJ#8 landslide.

Acknowledgments

References

Al-Rawabdeh A, He F, Moussa A, et al. (2016) Using an unmanned aerial vehicle-based digital imaging system to derive a 3D point cloud for landslide scarp recognition. Remote Sensing 8(2):95. https://doi.org/10.3390/rs8020095

Bardi F, Frodella W, Ciampalini A, et al. (2014) Integration between ground based and satellite SAR data in landslide mapping: the san Fratello case study. Geomorphology 223:45-60. https://doi.org/10.1016/j.geomorph.2014.06.025

Brideau MA, Sturzenegger M, Stead D, et al. (2012) Stability analysis of the 2007 Chehalis lake landslide based on long-range terrestrial photogrammetry and airborne LiDAR data. Landslides 9(1):75-91. https://doi.org/10.1007/s10346-011-0286-4

Brückl E, Brunner FK, Kraus K (2006) Kinematics of a deep-seated landslide derived from photogrammetric, GPS and geophysical data. Engineering Geology 88(3):149-159. https://doi.org/10.1016/j.enggeo.2006.09.004

Buckley SJ, Howell JS, Enge HD, et al. (2008) Terrestrial laser scanning in geology: data acq-uisition, processing and accuracy considerations. Journal of the Geological Society

165(3):625-638. https://doi.org/10.1144/0016-76492007-100

Chen ZC, Zhang B, Han YS, et al. (2014) Modeling accumulated volume of landslides using remote sensing and DTM data. Remote Sensing 6(2):1514-1537. https://doi.org/10.3390/rs6021514

Cigna F, Bianchini S, Casagli N (2013) How to assess landslide activity and intensity with persistent Scatterer interferometry (PSI): the PSI-based matrix approach. Landslides 10(3):267-283. https://doi.org/10.1007/s10346-012-0335-7

Derbyshire E, Meng XM, Kemp RA (1998) Provenance, transport and characteristics of modern aeolian dust in western Gansu Province, China, and interpretation of the Quaternary loess record. Journal of Arid Environments 39(3):497-516. https://doi.org/10.1006/jare.1997.0369

Derbyshire E (2001) Geological hazards in loess terrain, with particular reference to the loess re-gions of China. Earth-Science Reviews 54(1):231-260. https://doi.org/10.1016/S0012-8252(01)00050-2

Hsieh YC, Chan YC, Hu JC (2016) Digital elevation model differencing and error estimation from multipl-e sources: A case study from the Meiyuan Shan landslide in Taiwan. Remote Sensing 8(3):199. https://doi.org/10.3390/rs8030199

Dewitte O, Jasselette JC, Cornet Y, et al. (2008) Tracking landslide displacements by multi-temporal DTMs: A combined aerial stereophotogrammetric and LIDAR approach in western Belgium. Engineering Geology 99:11-22. https://doi.org/10.1016/j.enggeo.2008.02.006

Demoulin A (2006) Monitoring and mapping landslide displacements: a combined DGPS-stereophotogrammetric approach for detailed short- and long-term rate estimates. Terra Nova 18(4):290-298. https://doi.org/10.1111/j.1365-3121.2006.00692.x

Sebastian O, Irene M, Klaus DP, et al.(2012) Unmanned aerial vehicle (UAV) for monitoring soil erosion in Morocco. Remote Sensing 4(11):3390-3416. https://doi.org/10.3390/rs4113390

Fernández T, Pérez J, Cardenal J, et al. (2016) Analysis of Landslide Evolution Affecting Olive Groves Using UAV and Photogrammetric Techniques. Remote Sensing 8(10):837. https://doi.org/10.3390/rs8100837

Harwin S, Lucieer A (2012) Assessing the accuracy of Georeferenced point clouds produced via multi-view stereopsis from unmanned aerial vehicle (UAV) imagery. Remote Sensing 4(6):1573-1599. https://doi.org/10.3390/rs4061573

Kenner R, Bühler Y, Delaloye R, et al. (2014) Monitoring of high alpine mass movements combining laser scanning with digital airborne photogrammetry. Geomorphology 206(2):492-504. https://doi.org/10.1016/j.geomorph.2013.10.020

Jaboyedoff M, Oppikofer T, Abellán A, et al. (2012) Use of LIDAR in landslide investigations: a review. Nature Hazards 61:5-28. https://doi.org/10.1007/s11069-010-9634-2

Lucieer A, de Jong SM, Turner D (2014) Mapping landslide displacements using Structure from Motion (SfM) and image correlation of multi-temporal UAV photography. Progress in Physical Geography: Earth and Environment 38(1):97-116. https://doi.org/10.1177/0309133313515293

Mateos RM, Azañón JM, Roldán FJ, et al. (2016) The combined use of PSInSAR and UAV photogrammetry techniques for the analysis of the kinematics of a coastal landslide affecting an urban area (SE Spain). Landslides 14(2):743-754. https://doi.org/10.1007/s10346-016-0723-5

Malet JP, Maquaire O, Calais E (2002) The use of Global Positioning System techniques for the continuous monitoring of landslides: application to the Super-Sauze earthflow (Alpes-de-Haute-Provence, France). Geomorphology 43(1-2):33-54. https://doi.org/10.1016/S0169-555X(01)00098-8

Monserrat O, Moya J, Luzi G, et al. (2013) Non-interferometric GB-SAR measurement: application to the Vallcebre landslide (eastern Pyrenees,Spain). Nature Hazards and Earth System Science 13(7):1873-1887. https://doi.org/10.5194/nhess-13-1873-2013

Niethammer U, James MR, Rothmund S, et al. (2012) UAV-based remote sensing of the super-Sauze landslide: evaluation and results. Engineering Geology 128(11):2-11. https://doi.org/10.1016/j.enggeo.2011.03.012

Peng DL, Xu Q, Qi X, et al. (2016) Study on Early Recognition of Loess Landslides Based on Field Investigation. International Journal of Geohazards and Environment 2(2):35-52. https://doi.org/10.15273/ijge.2016.02.006

Peng DL, Xu Q, Liu FZ, et al. (2018) Distribution and failure modes of the landslides in Heitai terrace, China. Engineering Geology 236:97-110. https://doi.org/10.1016/j.enggeo.2017.09.016

Peng DL, Xu Q, Zhang XL, et al. (2019) Hydrological response of loess slopes with reference to widespread landslide events in the Heifangtai terrace, NW China. Journal of Asian Earth Sciences 171:259-276. https://doi.org/10.1016/j.jseaes.2018.12.003

Peng JB, Zhang FY, Wang GH (2017) Rapid loess flow slides in Heifangtai terrace, Gansu, China. Quarterly Journal of Engineering Geology and Hydrogeology 50(2):106-110. https://doi.org/10.1144/qjegh2016-065

Peternel T, Kumelj Š, Oštir K, et al. (2017) Monitoring the Potoška planina landslide (NW Slovenia) using UAV photogrammetry and tachymetric measurements. Landslides 14:395-406. https://doi.org/10.1007/s10346-016-0759-6

Prokešová R, Kardoš M, Medveďová A (2010) Landslide dynamics from high-resolution aerial p-hotographs: a case study from the Western Carpathians, Slovakia. Geomorphology 115(1-2):90-101. https://doi.org/10.1016/j.geomorph.2009.09.033

Prokop A, Panholzer H (2009) Assessing the capability of terrestrial laser scanning for monitoring slow moving landslides. Nature Hazards and Earth System Science 9(6):1921-1928. https://doi.org/10.5194/nhess-9-1921-2009

Qi X, Xu Q, Liu FZ (2018) Analysis of retrogressive loess flowslides in Heifangtai, China. Engineering Geology 236: 119-128. https://doi.org/10.1016/j.enggeo.2017.08.028

Qin RJ (2014) An object-based hierarchical method for change detection using unmanned aerial vehicle images. Remote Sensing 6(9):7911-7932. https://doi.org/10.3390/rs6097911

Federico R, Andrea C, Sara DC, et al. (2015) Exploitation of amplitude and phase of satellite SAR images for landslide mapping: the case of Montescaglioso (South Italy). Remote Sensing 7(11):14576-14596. https://doi.org/10.3390/rs71114576

Scaioni M, Longoni L, Melillo V, et al. (2014) Remote sensing for landslide investigations: An overview of recent achievements and perspectives. Remote Sensing 6(10):9600-9652. https://doi.org/10.3390/rs6109600

Squarzoni C, Delacourt C, Allemand P (2005) Differential single-frequency GPS monitoring of the La Valette landslide (French Alps). Engineering Geology 79(3-4):215-229. https://doi.org/10.1016/j.enggeo.2005.01.015

Stöcker C, Eltner A, Karrasch P (2015) Measuring gullies by synergetic application of UAV and close range photogrammetry - A case study from Andalusia, Spain. Catena 132:1-11. https://doi.org/10.1016/j.catena.2015.04.004

Tofani V, Raspini F, Catani F, et al. (2013) Persistent Scatterer interferometry (PSI) technique for landslide characterization and monitoring. Remote Sensing 5(3):1045-1065. https://doi.org/10.3390/rs5031045

Turner D, Lucieer A, de Jong SM (2015) Time series analysis of landslide dynamics using an Unmanned Aerial Vehicle (UAV). Remote Sensing 7(2):1736-1757. https://doi.org/10.3390/rs70201736

Xu L, Dai FC, Gong QM, et al. (2012) Irrigation-induced loess flow failure in Heifangtai Platform, North-West China. Environmental Earth Sciences 66(6):1707-1713.

Xu L, Dai FC, Tu XB, et al. (2014) Landslides in a loess platform, North-West China. Landslides 66(11):993-1005. https://doi.org/10.1007/s10346-013-0445-x

Yamagishi H, Marui H, Ayalew L, et al. (2004) Estimation of the sequence and size of the Tozawagawa landslide, Niigata, Japan, using aerial photographs. Landslides 1(4):299-303. https://doi.org/10.1007/s10346-004-0032-2

Yang IT, Park JK, Dong MK (2007) Monitoring the symptoms of landslide using the non-prism total station. KSCE Journal of Civil Engineering 11(6):293-301. https://doi.org/10.1007/BF02885900

Zhang M, Liu J (2010) Controlling factors of loess landslides in western China. Environmental Earth Sciences 59(8):1671-1680. https://doi.org/10.1007/s12665-009-0149-7